

## Short communication

# Influence of calcium substitution on structural, morphological and electrical conductivity properties of $\text{La}_{1-x}\text{Ca}_x\text{Ni}_{0.5}\text{Ti}_{0.5}\text{O}_3$ ( $x = 0.0, x = 0.2$ ) compounds for energy storage devices

S. Gharbi<sup>a,\*</sup>, Ahmadou Ly<sup>c</sup>, E. Dhahri<sup>a</sup>, R. Barille<sup>b</sup>, D. Lahem<sup>c</sup>, M. Debliquy<sup>d</sup>, M. Rguiti<sup>e,f</sup>

<sup>a</sup> Laboratoire de Physique Appliquée, Faculté des Sciences, Université de Sfax, 3000, Tunisie

<sup>b</sup> MOLTECH-Anjou, Laboratoire de Photonique, Université d'Angers, 2 Bd. Lavoisier, 49045 Angers, France

<sup>c</sup> Materia Nova R&D Center, Materials Science Unit, 56, Rue de l'Épargne, 7000-Mons, Belgium

<sup>d</sup> UMONS, Materials Science Department, 56, Rue de l'Épargne, 7000-Mons, Belgium

<sup>e</sup> Laboratoire de Matériaux Céramiques et de Mathématiques, F-59313 Valenciennes, France

<sup>f</sup> Université Polytechnique Hauts-de-France, INSA Hauts-de-France, CERAMATHS, France



## ARTICLE INFO

## Keywords:

Relaxation process  
Electrical conductivity  
Sol-gel method  
Nanomaterials  
Energy storage

## ABSTRACT

This paper explores the effect of calcium insertion on the physicochemical properties of  $\text{La}_{1-x}\text{Ca}_x\text{Ni}_{0.5}\text{Ti}_{0.5}\text{O}_3$  ( $x = 0.0$  (LNTO),  $x = 0.2$  (LCNTO)) compounds fabricated by the sol-gel process. The samples crystallize in an orthorhombic distorted structure with the  $Pnma$  space group. The purity and morphology of nano-grains were evaluated by SEM/ EDX analysis. The behaviors of the imaginary parts of the impedance ( $Z''$ ) show a dielectric relaxation phenomenon in the samples with activation energies close to those determined from the conductivity study. Nyquist diagrams are fitted using two circuits in series; each circuit consists of resistance in parallel with a CPE capacitance. The DC-conductivity enhances significantly with temperature confirming that our sample has a semiconductor behavior. The conduction mechanism was evaluated using the temperature dependence of the exponent Jonscher's power law parameter, which confirms the type of NSPT conduction mechanism for the compound LNTO and (NSPT) in zone I ( $T < 255$  K) and (OLPT) in zone II ( $T > 255$  K) for the LCNTO compound. The observed high conductivity indicates that our materials may be suitable for applications in energy storage devices.

## 1. Introduction

Nowadays, electronics are an integral part of our daily life (phones and laptops, household appliances, automobiles, etc.), and the presence of electronic components in all industrial sectors as well as in home automation has become commonplace. The capacitor is one of the passive components that takes center stage in these devices. Overall, it performs filtering or energy storage functions. There is a wide range of capacitor types available for a specific application based on their characteristics: the choice is made not only on the value of the desired capacitance but also on the nature of the dielectric, its behavior as a function of temperature, frequency range, and amplitude of the signal to be processed...etc. [1–4]. Among them, the family of complex oxides is derived from the perovskite structure  $\text{ABO}_3$ , demonstrating the richness of this family. Such a material can be modified by chemical doping and can contain both different cations at A and B sites. It is the nature and

proportions of these cations that governs the structural and electrical properties of the material [5,6]. The ease with which this structure can be modified gives these functional materials a wide range of applications: they are found, for example, in capacitors (dielectric properties DE), non-volatile memories (ferroelectric properties FE), infrared detectors (PE pyroelectric properties), sensors and actuators (PE piezoelectric properties), etc. Such materials can even perform several functions, sometimes simultaneously; they are then qualified as multi-functional materials [7,8].

From our previous studies, we found that the bismuth doping of the  $\text{La}_{1-x}\text{Bi}_x\text{Ni}_{0.5}\text{Ti}_{0.5}\text{O}_3$  ( $x = 0.0, x = 0.2$ ) nanocrystals prepared by the sol-gel method has a significant impact on the thermal, structural, morphological, electrical and dielectric properties [9,10]. Therefore, it will be interesting to correlate the electrical properties with the microstructure of the materials. For this purpose, we have used complex impedance spectroscopy which is a powerful tool to determine the

\* Corresponding author.

E-mail address: [azzouzi.sirine@outlook.com](mailto:azzouzi.sirine@outlook.com) (S. Gharbi).

<https://doi.org/10.1016/j.inoche.2022.109925>

Received 2 March 2022; Received in revised form 7 August 2022; Accepted 24 August 2022

Available online 30 August 2022

1387-7003/© 2022 Elsevier B.V. All rights reserved.

different relaxation processes present in grains, grain boundaries, and electrode interfaces of polycrystalline materials. Moreover, Titanium-substituted  $\text{LaNiO}_3$  was used as sensitive material for acetone detection with higher sensitivity, selectivity, and stability than other reported sensing materials [11]. The mechanism of acetone detection by  $\text{LaNi}_{1-x}\text{Ti}_x\text{O}_3$  was explained by the structural change characterized by XPS analysis [11]. In addition, the same authors have prepared and used composites with perovskite  $\text{LaNi}_{0.5}\text{Ti}_{0.5}\text{O}_3$  (LNT) for various applications. Among these composites: perovskite-type composite oxide  $\text{LaNi}_{0.5}\text{Ti}_{0.5}\text{O}_3\text{-NiFe}_2\text{O}_4$  was prepared by sol-gel method and used to build an electrochemical biosensor for glucose detection [11] and the composite  $\text{LaNi}_{0.5}\text{Ti}_{0.5}\text{O}_3 / \text{CoFe}_2\text{O}_4$  (LNT - CFO) [12] was an excellent sensitive material for the detection of  $\text{H}_2\text{O}_2$ . In addition, with a  $\text{LaNi}_{0.5}\text{Ti}_{0.5}\text{O}_3$  perovskite, Wang et al. constructed an electrochemical sensor for amino acids based on a modified carbon paste electrode [13].

In recent years, iron-substituted  $\text{Sr}_{0.5}\text{Ba}_{0.5}\text{TiO}_3$  (SBT) is considered a good potential candidate applicable to multiferroic device applications because there is the simultaneous existence of magnetic and ferroelectric properties [14]. In addition, with a perovskite  $\text{BaTiO}_3$  they report the low temperature synthesis of  $\text{BaTiO}_3$  using sol-gel auto-combustion method and results of the study of structural, infrared and dielectric properties are reported [15]. In addition, they manufactured nanoceramics of barium titanate doped with  $\text{La}^{3+}$  using the technique of

automatic combustion soil-gel and to study the role of  $\text{La}^{3+}$  doping on the structure and morphological properties. These results show that A-doped  $\text{BaTiO}_3$  nanoceramics are promising candidates for spintronic applications [16]. In addition, they fabricate the  $\text{TiO}_2$  nanophotocatalyst doped Fe by a simple and cost-effective ground-gel auto-ignition pathway by following the Green Synthesis Approach for nanotechnology applications in wastewater treatment [17].

In the current work, our goal is to prepare the Ca-substituted nanomaterials with a low concentration of calcium to improve the electrical conductivity in  $\text{LaNi}_{0.5}\text{Ti}_{0.5}\text{O}_3$ . We performed structural analysis to study the effects on the lattice parameter and lattice strain crystalline size, of the nanomaterials. In order to investigate the electrical properties of the compound, we used complex impedance spectroscopy. This procedure characterizes the electrical conductivity of the sample and separates several contributions (grains and grain boundaries) that may represent the material.

## 2. Experimental procedures:

### 2.1. Nanoparticles preparation:

The  $\text{La}_{1-x}\text{Ca}_x\text{Ni}_{0.5}\text{Ti}_{0.5}\text{O}_3$  ( $x = 0.0$  (LNTO) and  $x = 0.2$  (LCNTO)) nanopowders are prepared by sol-gel technique. We used the following

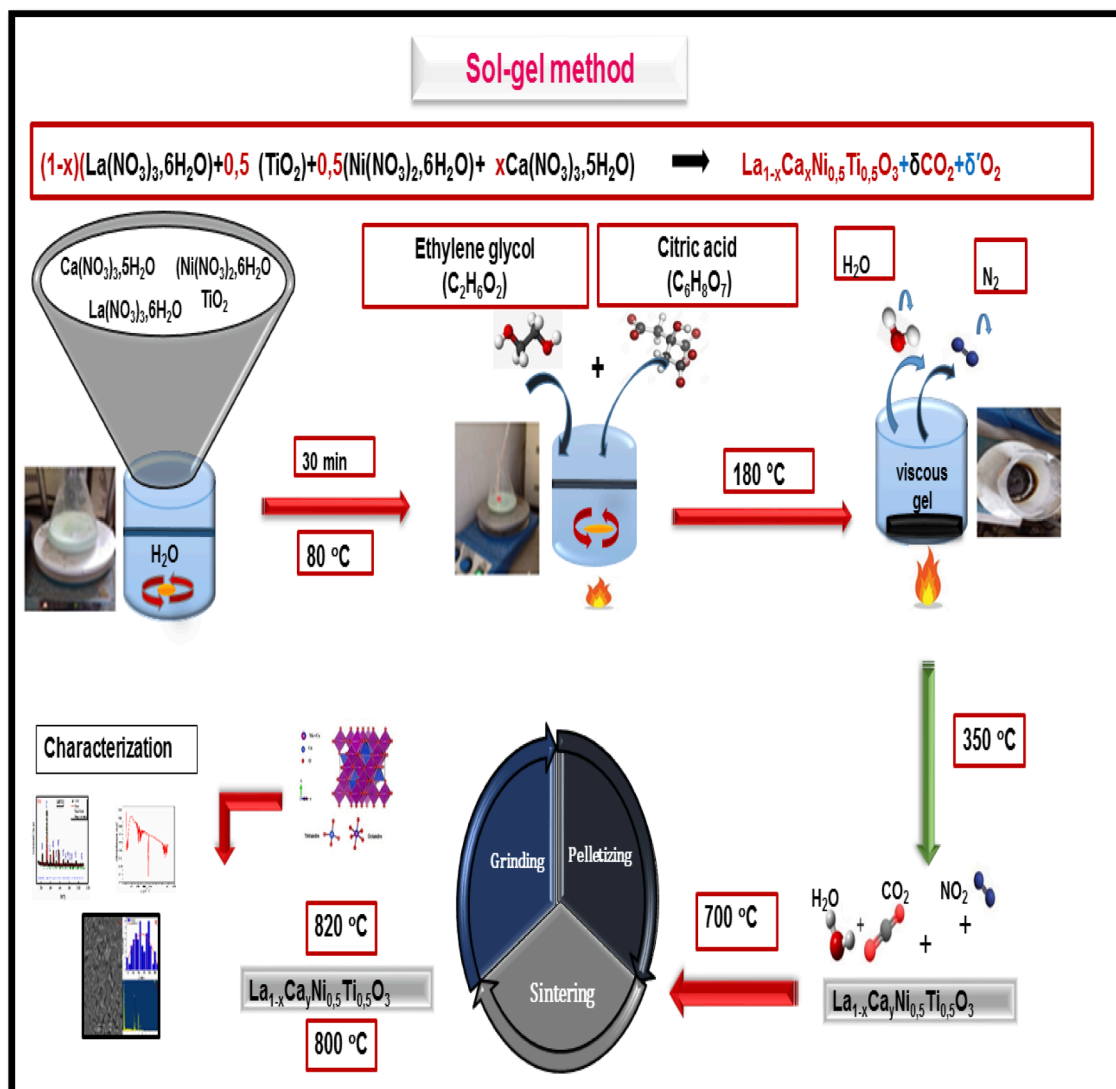


Fig. 1. Synthesis steps by the sol-gel method of the LNTO and LCNTO compounds sintering at different temperatures.

precursors: La (NO<sub>3</sub>)<sub>3</sub> 6H<sub>2</sub>O, Calcium nitrate (Ca(NO<sub>3</sub>)<sub>2</sub> 4H<sub>2</sub>O), Nickel nitrate ((Ni(NO<sub>3</sub>)<sub>2</sub> 6H<sub>2</sub>O), titanium oxide TiO<sub>2</sub>, ethylene glycol (C<sub>2</sub>H<sub>6</sub>O<sub>2</sub>) and citric Acid (C<sub>6</sub>H<sub>8</sub>O<sub>7</sub>). The quantities of precursors to prepare our samples are computed using the subsequent reaction equation:

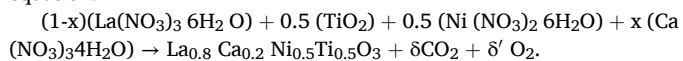


Fig. 1 exhibits the different synthetic steps of the samples. During the preparation, the stoichiometric amounts of these nitrates were first dissolved in distilled water by stirring regularly at room temperature on a hot plate. Citric acid (metal complex agent) and ethylene glycol are then added to the solution mixture which has been heated to 80° C until complete dissolution of the precursors and evaporation of water. The solution obtained is brought to 180° C until a viscous gel is obtained. Then, the gel was dried at 300° C and the ground powder was calcined at 400° C for 12 h. To remove the organic phases, the powder was subjected to annealing at 700° C for 12 h. Then the obtained product was put in the form of pellets, 12 mm in diameter and 1.6 mm in thickness, using a uniaxial pressure system with a pressure of 5 tons. Then the compounds under investigation were grounded and warmed up at 800° C for 24 h. The obtained product was finely ground and pelletized to undergo heat treatment at 820° C for 24 h.

## 2.2. Characterization of materials:

The structure of the compound annealed at 820° C was characterized by XRD. The measurement was made at 300 K using a Bruker 8D Advance X-ray powder diffractometer in the range of 15° to 110°, with CuK<sub>α1</sub> radiation (λ = 1.5406 Å) and a step size of 0.02°. Surface morphological characterization and chemical compositions of synthesized samples were investigated using a scanning electron microscopy (MEB) Hitachi S3500 Micro-analysis EDS, Kevex (132 KeV) equipped with Energy Dispersive X-ray (EDX) micro analyzer. For electrical measurements, both parallel edges of the pellets are covered with silver paste as electrodes. The impedance measurement is connected to the computer by using an impedance analyzer (HP 4194), the frequency range is 100–10<sup>6</sup> Hz, and the temperature range is 233 K to 313 K.

## 3. Results and discussions:

### 3.1. Thermal analysis

The ATG thermogravimetric curves and the typical DSC calorimetric analysis were reported in Fig. 2. The LaNi<sub>0.5</sub>Ti<sub>0.5</sub>O<sub>3</sub> (LNTO) compound ATG curve (Fig. 2 (a)) is divided into four regions, with different processes taking place in each region, namely 25–150° C, 150–336° C, 336–600° C and 600–800° C. Whereas for La<sub>0.2</sub>Ca<sub>0.2</sub>Ni<sub>0.5</sub>Ti<sub>0.5</sub>O<sub>3</sub> (LCNTO), the curve obtained by ATG can be divided into three regions: 28–276° C, 276–435° C and 435–800° C for LCNTO.

The first temperature region corresponds to a weight loss of approximately 1.05 % (25–150° C) and 0.5 % (28–276° C) for the three LNTO and LCNTO compounds, respectively. These mass losses are due to the removal of water molecules for the three compounds [18]. However, the LNTO compound shows a second region in the temperature range of 150 to 600° C, where complex decomposition of organic species and nitrates occurs. There is a start and end temperature of decomposition between 150 and 336° C associated with a weight loss of about 0.87 %, this is due to the presence of species of nitrates/ or intermediate oxides or citric acid. This effect is also present by another initial and final decomposition between 336 and 600° C with a weight loss of about 0.62 %, leading to the transformation of intermediate species into oxides [19]. For the LCNTO compound, a weight loss of about 0.38 % in the second region (276–435° C) is due to the decomposition of organic species and nitrates present in both samples. The third region between temperatures 600–800° C for the LNTO compound and 435–800° C for the LCNTO compound shows no mass loss, indicating the formation of

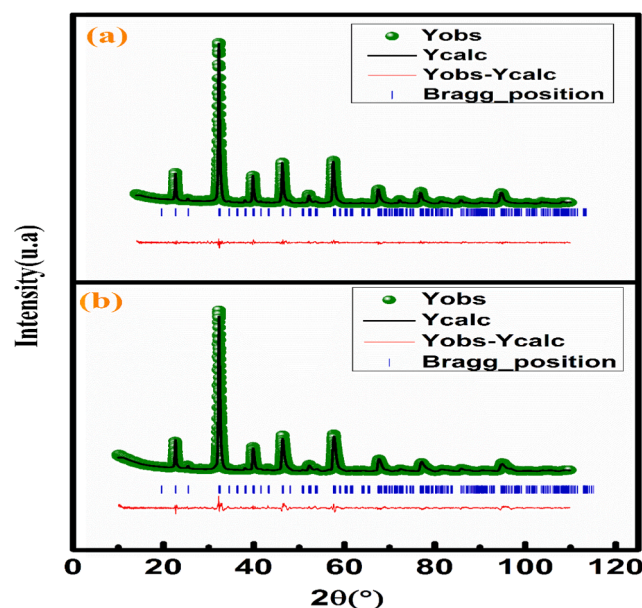


Fig. 2. Refined X-ray diffraction patterns of Sol-Gel for LNTO (a) and LCNTO (b) samples.

the final product giving a monophasic perovskite crystallization of our samples [20].

Fig. 2 (b) shows the scanning calorimetric analysis (DSC) of the LNTO and LCNTO compounds. Two major endothermic peaks were observed at approximately 408° C and 334° C for LNTO and LCNTO, respectively. The major endothermic peaks of approximately 408° C for the LNTO compound and 334° C for the LCNTO compound in the DSC chart are also found due to the thermal effect of the decomposition of precursors.

### 3.2. X-ray diffraction investigation:

In order to determine the phases present in our samples and verify their purity, an X-ray diffraction analysis was performed using a Bruker D8 diffractometer equipped with a copper anticathode (λ = 1.54056 Å). The recording of the X-ray powder diagrams was carried out in the angular range varying from 15° to 110° with a step of 0.02°. In Fig. 3, we have illustrated the result of the refinement of the LNTO and LCNTO samples. DRX data were analyzed by the Rietveld method using the Fullprof program. All compounds crystallize in the same orthorhombic structure with the *Pnma* space group. The summary of the structural parameters, the bond lengths, and bond angles obtained for the two compounds are given in Table 1.

The theoretical X-ray density of the compounds is computed by employing the subsequent equation[21]:

$$d_{\text{theor}} = \frac{Z \times M}{N_A \times V_p} \quad (1)$$

The experimental density is given by this equation:

$$d_{\text{exp}} = \frac{m}{V} \quad (2)$$

where, *M* represents the molecular mass, *N<sub>A</sub>* represents the Avogadro number, *V<sub>p</sub>* represents the volume determined from the XRD results, *m* is the mass of the pellet and *V* is the volume of the pellet. The values of the theoretical X-ray density (*d<sub>theor</sub>*) and the experimental density (*d<sub>exp</sub>*) are listed in Table 1.

In hypothetical terms, all particles are spherical, and the specific surface area (*S*) is computed according to the relationship  $S = 6000 / D_{W-H} \cdot d_{\text{exp}}$ , where the specific surface area *S* in m<sup>2</sup>/g, *D<sub>W-H</sub>* represents the diameter of the particle in nm, and *d<sub>exp</sub>* experimental density of the particle in g/cm<sup>3</sup>. The parameter *S* is highlighted in Table 1.

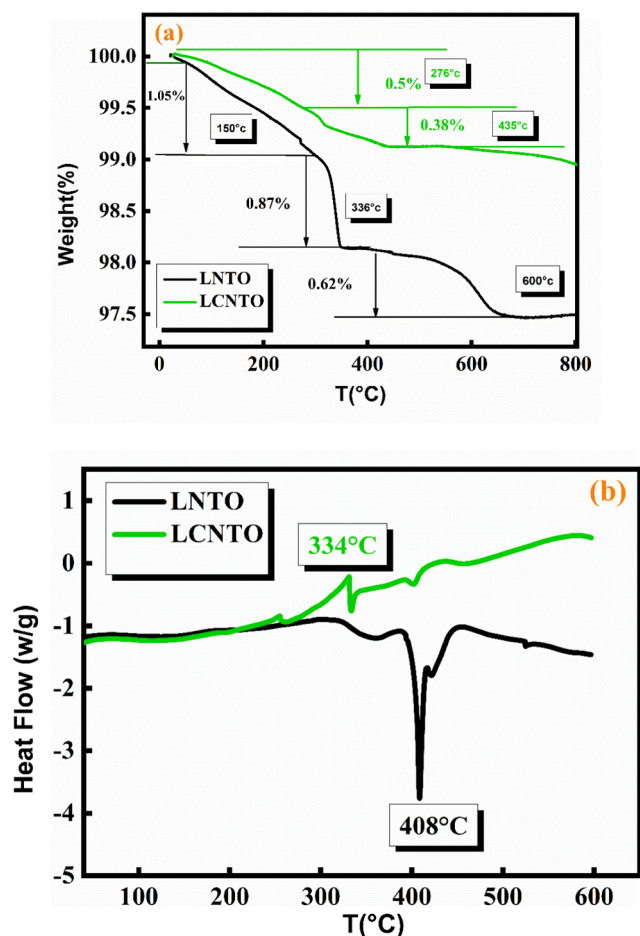


Fig. 3. (a) Thermogravimetric analysis (TGA) and (b) Differential Scanning Calorimetry (DSC) curves of the LNTO and LCNTO compounds.

Table 1

The Results of Rietveld refinements for LNTO and LCNTO nanopowders.

Samples		LNTO	LCNTO
Space group		<i>Pnma</i>	<i>Pnma</i>
Cell parameters	<i>a</i> (Å)	5.502(4)	5.528(2)
	<i>b</i> (Å)	7.842(15)	7.801(5)
	<i>c</i> (Å)	5.546(10)	5.522(8)
	<i>V</i> (Å <sup>3</sup> )	239.378(0.053)	238.13(7)
Agreement Factors	<i>R<sub>p</sub></i> (%)	12.3	11.1
	<i>R<sub>wp</sub></i> (%)	12.9	15.0
	<i>R<sub>f</sub></i> (%)	2.30	2.19
	$\chi^2$ (%)	1.63	3.89
<i>&lt;Ni-O<sub>1</sub>&gt;</i> (Å)	1.999(5)	1.999(5)	
<i>&lt;Ni-O<sub>2</sub>&gt;</i> (Å)	2.066(19)	2.06(6)	
<i>&lt;Ni-O<sub>1</sub>-Ni&gt;</i> (°)	157.5(2)	157.52(1)	
<i>&lt;Ni-O<sub>2</sub>-Ni&gt;</i> (°)	160.0(8)	160.0(8)	
<i>d<sub>theor</sub></i> (g/cm <sup>3</sup> )	6.666	6.614	
<i>d<sub>exp</sub></i> (g/cm <sup>3</sup> )	6.1136	6.112	
<i>S</i> (m <sup>2</sup> /g)	52	16	

### 3.3. Morphological study

The surface morphologies of the LNTO and LCNTO were studied by the scanning electron microscope (SEM). The compounds microscopy (SEM) images are exhibited in Fig. 4 (a) and (b). These images display a relatively uniform particle size distribution and can be agglomerated, declaring that the sol-gel method is a good method for elaborating uniform and dense powders.

### 3.4. Energy dispersive X-ray spectroscopy, EDS analysis

To check the elemental compositions of our samples, we employed the energy dispersive X-ray Spectroscopy (EDX) (Fig. 4 (c) and (d)). The results of the EDX analysis are introduced in Fig. 4. We note the existence of characteristic peaks of all chemical elements (La, Ca, Ni, O and Ti) initially introduced during the preparations. In fact, Fig. 4 (c) and (d) indicate the presence of all the initial elements, verifying that no loss of an element occurred during the reactions without the presence of impurity elements. The elemental composition values are in excellent agreement with the nominal composition, confirming that there is no loss of integrated elements after sintering.

### 3.5. Complex impedance evaluation

In order to study the relaxation process for the LNTO and LCNTO nanomaterials, we examined the real part ( $Z'$ ) and imaginary part ( $Z''$ ) of the complex electrical impedance at various temperatures in the frequency range of  $10^2$ - $10^6$  Hz. The complex impedance of dielectric nanomaterials is described by:

$$Z^* = Z' - jZ'' \quad (3)$$

With,  $Z'$  and  $Z''$  are the real and imaginary parts of the complex impedance, respectively.

#### 3.5.1. Study of the real part ( $Z'$ ) of impedance

The measured  $Z'$  value of the elaborated LNTO and LCNTO compounds was plotted in Fig. 5 (a) and (b).  $Z'$  value decreases when the temperature increases which specified the increase in conductivity[22]. It is clear that  $Z'$  remains almost constant in the low-frequency range and subsequently decreases with the frequency increase and achieves a small value, irrespective of frequencies. This is consistent with the results of perovskite compounds[23]. Indeed, this change may be linked to a decrease in the density of trapped charges and the enhancement in the mobility of charge carrier[24]. In addition, the merge of the  $Z'$  plots at high frequency confirms the presence of space charges, which is advantageous due to the reduced barrier behaviors of nanomaterials[25].

#### 3.5.2. Study of imaginary part ( $Z''$ ) of impedance

In Fig. 5 (c) and (d), the  $Z''$  of the samples are plotted as a function of the frequency in the temperature range between 233 and 313 K. It can be seen that there are relaxation peaks, corresponding to the inflection points observed in the  $Z$  plots. As the temperature increases, the peaks shift to higher frequencies, thus confirming the relaxation mechanism by thermal activation. As though, it is immediately proportional to the mean mobility outlined by Shah and his group, we conclude that charge carriers will shift rapidly with temperatures[26]. The value of  $Z''$  decreased for an additional increase in frequency, confirming the presence of a relaxation mechanism in the prepared samples[27]. Furthermore, at high frequencies, due to the accumulation of space charges in the compounds, the  $Z''$  curve will merge and become a frequency and temperature independent curve[28]. This merging of the curves is explained by the fact that the space charge does not need further time to relax in the high-frequency region, which changes its polarization as the frequency increases. In order to determine the activation energy, the change of  $\ln(f_{max})$  and the corresponding frequency of the maximum  $Z''$  are plotted according to Arrhenius' law:

$$f_{max} = f_0 e^{-\frac{E_a}{k_B T}} \quad (4)$$

Where  $f_0$  is the pre-exponential term,  $E_a$  is the activation energy and  $k_B$  is the Boltzmann constant. Fig. 6 (a) and (b) show the  $\ln(f_{max})$  vs  $1000/T$ . The adjustment results and proved that the activation energy values  $E_a$  are 0.404 eV for LNTO are presented for LCNTO in the region (R-I),  $E_a$  is 0.530 eV and 0.198 eV in the region (R-II).

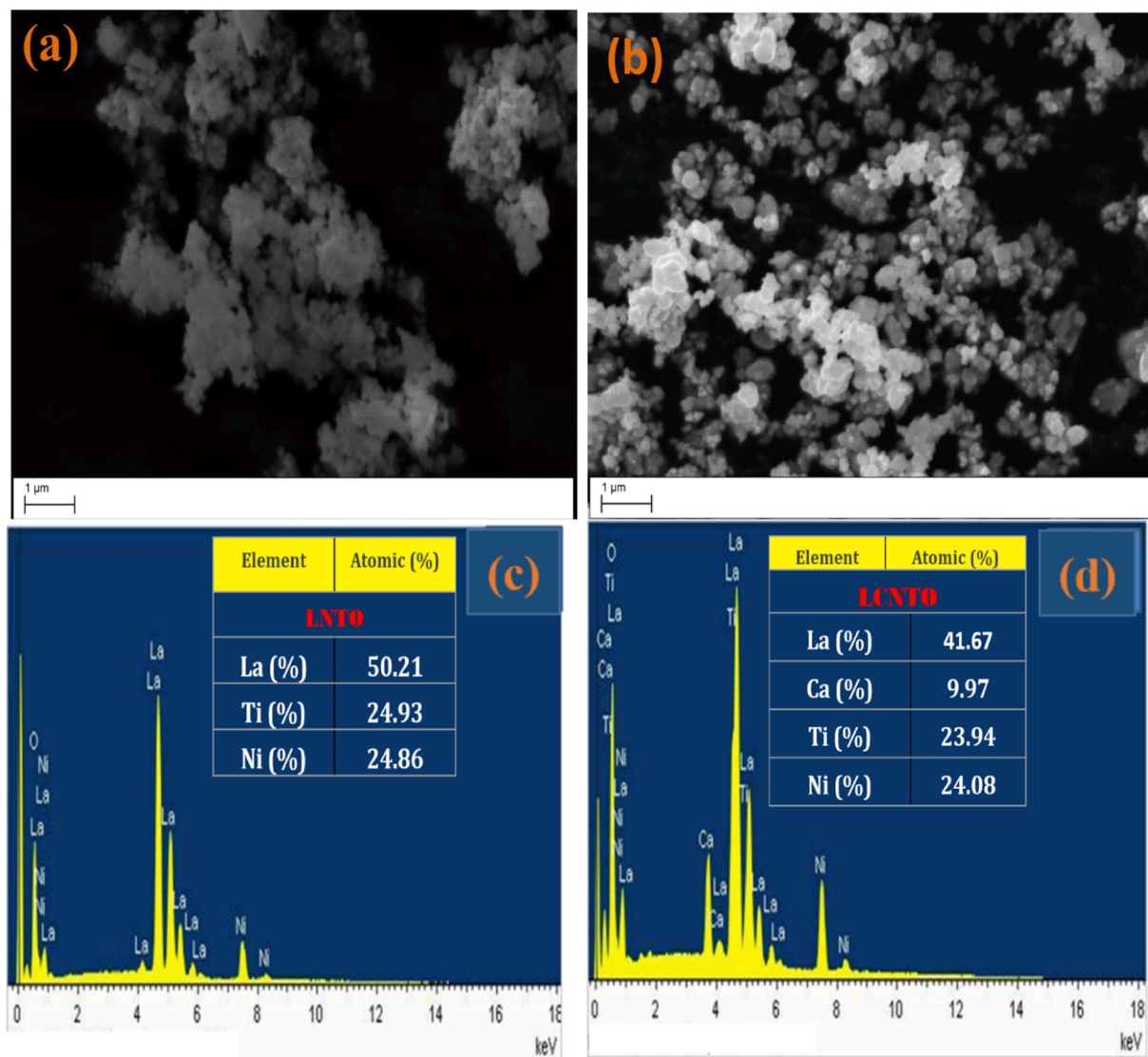


Fig. 4. (a), (b) SEM images and (c) (d) Spectra of chemical analysis of LNTO and LCNTO nanoparticles.

### 3.5.3. Assessment of the Nyquist spectra

In order to determine the contribution of grains and grain boundaries to the electrical conductivity, we represented the impedance in the Nyquist plane. The Nyquist diagram includes in tracing the  $Z''$  as a function of the  $Z'$  in an orthonormal Cartesian coordinate system. The graphic representation is usually a series of arcs, and each arc may be related to a contribution of the constituent material[29] (grains, electrodes, grain boundaries, etc.). Moreover, we conduct physical studies on the elements in the equivalent circuit configuration to determine the properties of dielectric relaxation in the compound, so that the experimental data can be adapted to various pattern[30], specifically the Debye, Cole–Cole, Davidson–Cole, and/or Havriliak–Negami models. The Nyquist diagrams for the LNTO and LCNTO compounds, which are characterized at different temperatures, are presented in Fig. 7 (a) and (b). The figures present semicircles starting from the origin. The mentioned decentralization confirms a non-Debye relaxation mechanism[31]. We noted the diameter of the semicircle whose radius of curvature decreases due to the increase in temperature. This behavior specifies the thermally activated conduction process[32]. Using the Z-view program, the fit is established by modulating the experimental results with both combinations of  $R_g // Q_g$  and  $R_{gb} // Q_{gb}$ , thereby verifying the existence of the two contributions (grains and grain boundaries). The values of all adjusted parameters ( $R_g$ ,  $R_{gb}$ , CPE (g), CPE

(gb),  $\alpha$  (g), and  $\alpha$  (gb)) are listed in Table 2. It is pointed out from the table that the resistance value of boundary grains and grains rises with rising temperature, which can be clarified by the rise in charge carrier mobility that provides to the conduction mechanism.

### 3.6. Ac-conductivity and conduction mechanism

Several mechanisms can provide electrical conductivity. Among these mechanisms, intrinsic charge carriers, lattice energy, defects, and impurities are included. To fully comprehend the conduction compartment of the parameters that can control this process of the samples, measurements of electrical conductivity are made. Subsequently, it is considered to investigate this quantity to evaluate it for appropriate applications. The total conductivity of the LNTO and LCNTO samples was computed with the following equation:

$$\sigma = G \frac{t}{S} \quad (5)$$

with,  $G$ ,  $S$  and  $t$  are respectively the electrical conductance, the area of cross-section of the pellet, and the thickness. The variation of the alternative conductivity versus the frequency of the LNTO and LCNTO materials was investigated in the temperature span of 233–313 K. We noted that the conductivity rises with rising temperature, indicating that

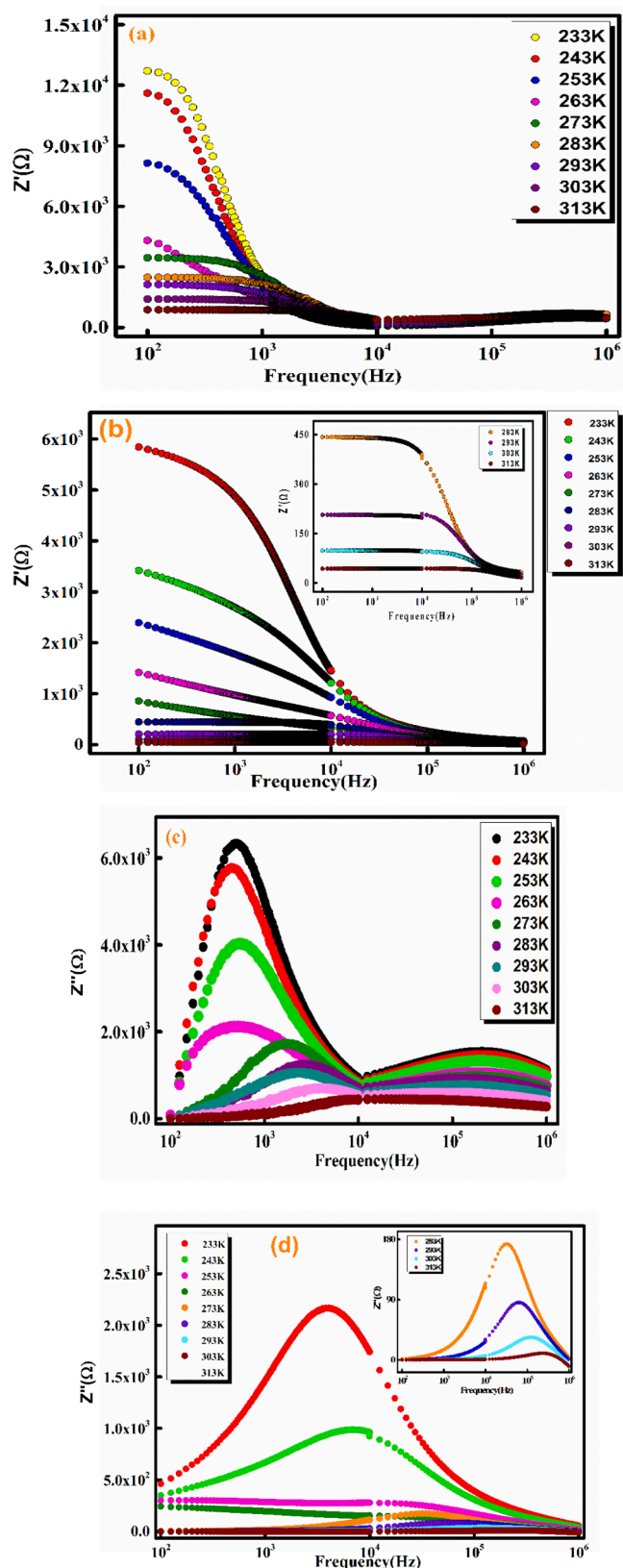


Fig. 5. The variation of real part of the impedance ( $Z'$ ) of LNTO (a) and LCNTO (b) compounds as a function of frequency for different temperatures. The variation of imaginary part of the impedance ( $Z''$ ) of LNTO (c) and LCNTO (d) compounds as a function of frequency for different temperatures.

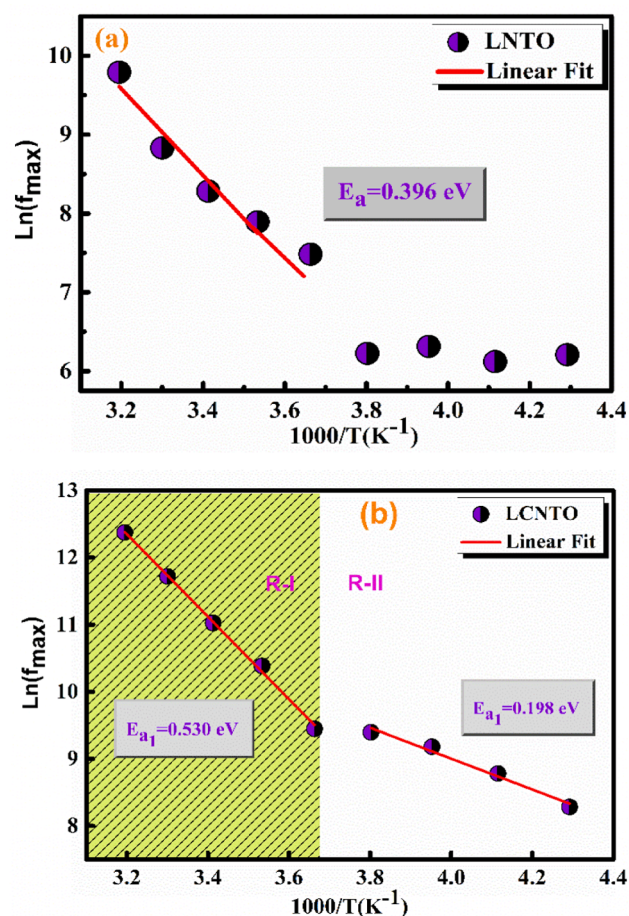


Fig. 6. The variation of  $\ln(f_{\max})$  as a function of  $1000/T$  of LNTO (a) and LCNTO (b) samples.

the conduction mechanism in the LNTO and LCNTO nanoparticles was thermally activated. We can identify two regions for conductivity as a function of the frequency [33]. For the low-frequency zone (100 Hz to  $10^4$  Hz), the conductivity is constant and independent of the frequency for a given temperature, which describes the uniform compartment owing to direct current conductivity ( $\sigma_{dc}$ ). In addition, the perovskite materials have well-conductive grains encircled by badly conductive grain boundaries and their activity is higher at lower frequencies. This effect conducts to a bad conductivity due to a weak electron jump in this region [34]. For the second region ( $10^4$  Hz to  $10^6$  Hz), when the frequency increases, the conductivity shows an important rise. This is owing to the existence of more charge carriers and more processes of jumping charge carriers among consecutive sites in the material. Then, this phenomenon exhibits dispersive compartment, inducing AC conduction conductivity ( $\sigma_{ac}$ ). In fact, Fig. 8 (a) and (b) prove that the alternating current conductivity of the samples obeys Jonscher's power law behavior, which is specified by [35]:

$$\sigma(\omega) = \sigma_{ac} + \sigma_{dc} = \sigma_{dc} + A\omega^S \quad (6)$$

where  $\sigma_{dc}$  represents the direct current conductivity,  $A$  represents a temperature dependent constant,  $\omega$  represents the angular frequency  $\omega = 2\pi f$  and " $S$ " is the degree of interaction among mobile ions and the lattices [36]. It notes that the electrical conductivity increases at all temperatures in Ca-substituted compounds much better than LNTO (see Fig. 8 (a) and (b) and Table 3), this increase is due to the higher electrical conductivity of Calcium ( $29.8 \cdot 10^6 \text{ S}\cdot\text{m}^{-1}$ ) compared to Lanthanum ( $1.26 \cdot 10^6 \text{ S}\cdot\text{m}^{-1}$ ). The observed high conductivity values indicate that our samples may be suitable for technological applications such as electronic chips, energy storage capacitors, electrical devices, gas

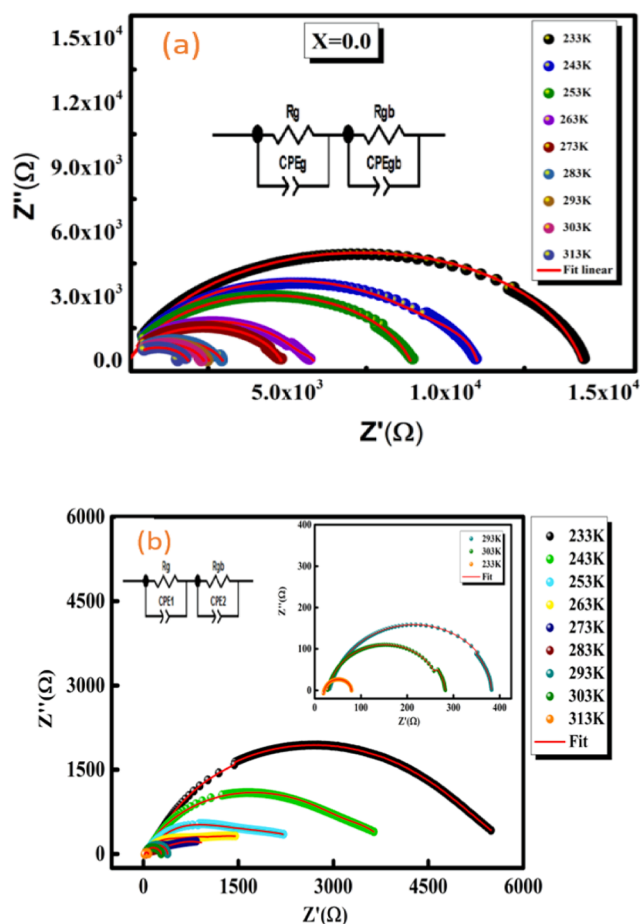


Fig. 7. The Complex impedance plots of  $Z'$  versus  $Z''$  (Nyquist plot) at different temperatures of LNTO (a) and LCNTO (b) samples.

Table 2

Values of electrical parameters deduced from the complex diagram at selected temperatures for LNTO and LCNTO samples.

T (K)	$R_g$ ( $10^3 \Omega$ )	$Q \times 10^{-5}$ (F)	$\alpha$	$R_{gb}$ ( $10^7 \Omega$ )	$Q \times 10^{-6}$ (F)	$\alpha$
LNTO						
233 K	80	50	0.81	1.8	5.7	0.19
243 k	69	9	0.82	1.03	9	0.40
253 k	60	5	0.79	0.69	9.1	0.45
263 K	20	0.5	0.75	0.51	10	0.49
273 K	19	0.2	0.72	0.15	20	0.62
283 K	9	50	0.71	0.13	0.7	0.70
293 K	3	90	0.75	0.057	5	0.76
303 K	2	50	0.75	0.0359	4	0.82
313 K	2	40	0.67	0.0152	3.2	0.78
LCNTO						
233 K	520	9	0.72	5300	5.55	0.78
243 k	400	60	0.93	3370	5.40	0.72
253 k	390	260	0.99	2200	0.46	0.49
263 K	350	900	0.99	1350	0.99	0.52
273 K	320	1000	0.88	1290	0.2	0.69
283 K	300	1100	0.82	1190	0.7	0.72
293 K	280	1180	0.75	1169	0.5	0.73
303 K	250	1254	0.65	1120	0.4	0.83
313 K	200	1390	0.69	1096	0.32	0.75

detection and resonant wave devices..

The value of  $S$  can be specified by fitting the experimental data  $\sigma(\omega)$  with equation (6). The results of the adjustment at various temperatures are put together in Table 3.

Fig. 9 (a) and (b) exhibit the change of the exponent ( $S$ ) with

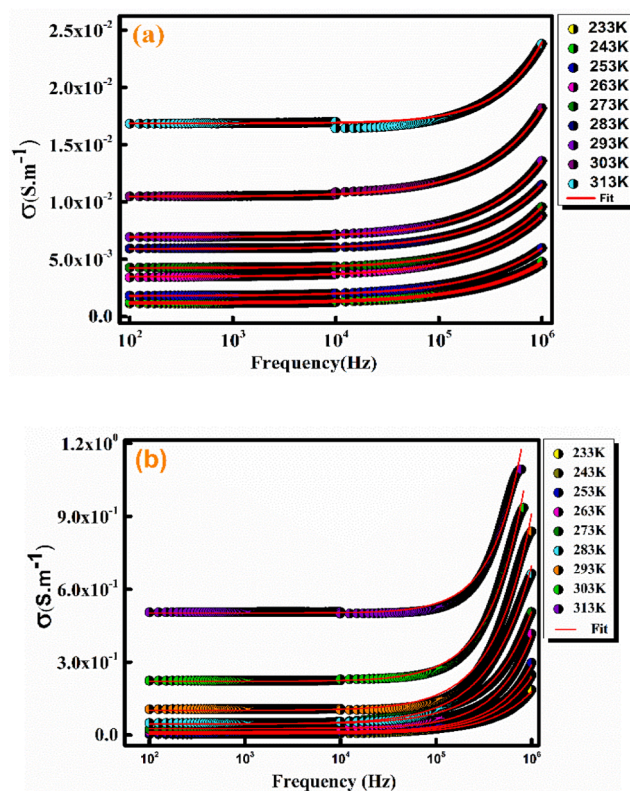


Fig. 8. The variation of the electrical conductivity versus the frequency at different temperatures of LNTO (a) and LCNTO (b) compounds.

Table 3

Refinement parameters using Jonsher model for LNTO and LCNTO compounds.

Samples	$T_0$ (K)	$\xi$ (Å)	$N(E_F)$ ( $eV^{-1} cm^{-3}$ )
LNTO	$4.72 \times 10^8$	5.3	$3.54 \times 10^{33}$
LCNTO	$2.96 \times 10^9$	5.3	$2.01 \times 10^{17}$

temperature, proving the evolution of the conductivity process. In the perovskite samples, the parameter  $S$  has a very important role in determining the conduction mechanism. It is well known, according to Funke and al. [37], that if  $S < 1$ , the charge carriers receive a translation displacement with a sudden hopping, and when  $S > 1$  a located jump of the species occurs. In our case, the compounds LNTO and LCNTO have  $S$  higher than 1 so a located jump of the species occurs. Four conduction models can help to distinguish the behavior of  $S$  (t):

- The Related barrier jumping model (CBH) ( $S$  decreases with rising temperature) [38].
- The Quantum Mechanical Tunnel Model (QMT) ( $S \approx 0.8$ ) [39]
- The Non-overlapping Small Polaron Tunneling (NSPT) ( $S$  raises with temperature) [40].
- The Overlapping Large-Polaron Tunneling (OLPT) model ( $S$  decreases and then rises with rising temperature)[41].

In our case for the LNTO compound, " $S$ " increases when the temperature increases. The ac-conductivity follows the Non-overlapping Small Polaron Tunneling (NSPT) where the parameter " $S$ " is established by equation [40]:

$$s(T) = 1 + \frac{4}{\frac{W_m}{k_B T} + Ln(w\tau_0)} \quad (7)$$

With,  $W_m$  represents the bonding energy of the carrier in its localized

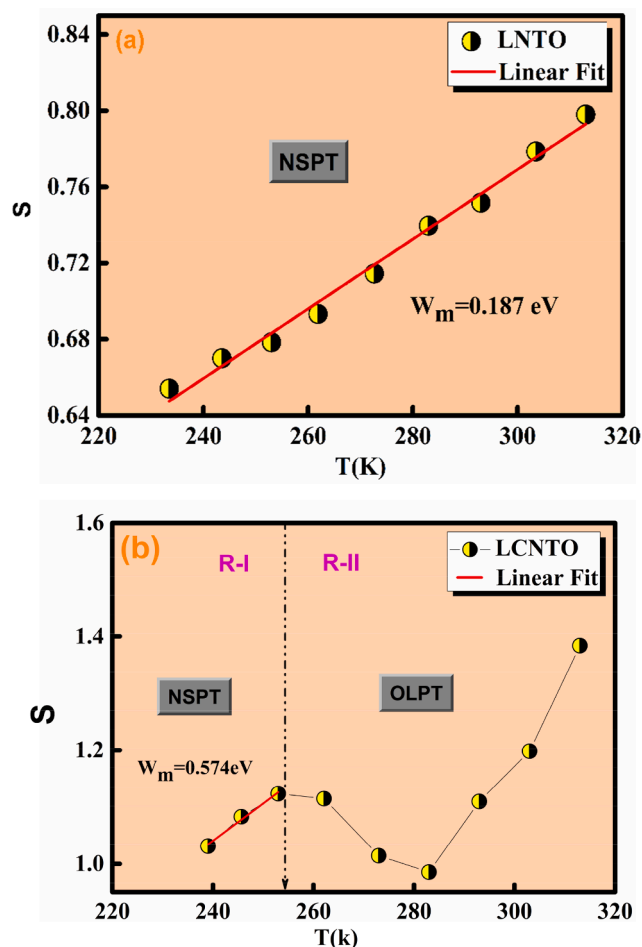


Fig. 9. The variation of the exponents  $S$  as a function of temperature of LNTO (a) and LCNTO (b) compounds.

sites,  $T$  is the temperature,  $k_B$  represents the Boltzmann constant,  $\omega$  corresponds to the angular frequency and  $\tau_0$  corresponding to the relaxation time.

In this equation,  $W_m$  is the polaron hopping energy. For higher values of  $W_m/k_B T$ , “ $s$ ” can be given by:

$$s(T) = 1 + \frac{4k_B T}{w_m} \quad (8)$$

From the slope of the curve of “ $s$ ” versus the temperature, the value of  $W_m$  for the LNTO compound is computed. The average binding energy  $W_m$  of the studied sample is assessed at around 0.187 eV.

For the LCNTO compound,  $S$  displays two behaviors:

- From 220 to 255 K,  $S$  rise with the rising temperature. Therefore, this change can be specified by the NSPT model, according to the slope of the curve of  $S$  versus temperature, the value of  $W_m$  for the LCNTO compound is calculated. The mean binding energy  $W_m$  of the studied sample is estimated about 0.574 eV.
- From 255 to 313 K, the values of “ $S$ ” decrease with rising temperatures to a minimum value and then rise when the temperatures rise. Therefore, the OLPT model is the most suitable model for specifying the conduction process. In this category of conduction, it is assumed that the larger polaron wells at two locations overlap, so they reduce the polaron jump energy, which is described by:

$$W_H = W_{H0} \left(1 - \frac{r_p}{R}\right) \quad (9)$$

With,  $W_{H0}$ ,  $r_p$ , and  $R$  are, respectively, related to the activation

energy, the radius of a large Polaron, and the inter-site separation. The relationship between the power parameters and temperature of the OLPT process can be described by: [41].

$$S = 1 - \frac{8\alpha R\omega + \frac{6W_{H0}r_p}{k_B T R\omega}}{(2\alpha R\omega + \frac{W_{H0}r_p}{k_B T R\omega})^2} \quad (10)$$

With,  $\alpha$  represents the spatial extent of the polaron,  $R\omega$  represents the jumping length at the angular frequency  $\omega$ ,  $T$  represents the temperature and  $k_B$  represents the Boltzmann constant. The OLPT happens when the polaron distortion clouds overlap. The title of “large polaron” is due to the spatial extent of the polaron in relation to interatomic distances. To compute the activation energy, it is necessary to plot the relationship between the variations  $\ln(\sigma_{dc}T)$  and the reciprocal temperature (Fig. 10 (a) and (b)). The experimental data of direct current conductivity has been well plotted by Mott and Davis Law [42], which specifies SPH:

$$\sigma_{dc}T = \sigma_0 \exp\left(-\frac{E_a}{k_B T}\right) \quad (11)$$

With  $E_a$ ,  $\sigma_0$ ,  $k_B$  and  $T$  are activation energy, pre-exponential factor, Boltzmann constant and absolute temperature, respectively. The curve of the SPH exhibits that the conductivity rises in temperature, verifying that the conduction process has been thermally activated. We use equation (11) to calculate the  $E_a$  value of the slope of the linear fit plot. The obtained value is 0.376 for samples LNTO. For LCNTO, for the R-I region and R-II region, the gained values are 0.634 eV and 0.323 eV, respectively.

The experimental conductivity  $\sigma_{dc}$  value is examined with a change range jump (VRH) model, at bass temperatures. The model is specified by the following equation [43]:

$$\sigma_{dc} = \sigma_0 \exp\left(-\frac{T_0}{T}\right)^{-0.25} \quad (12)$$

With,  $\sigma_0$  is a pre-exponential factor,  $T$  is the absolute temperature and  $T_0$  is the Mott temperature. The plot of  $\ln(\sigma_{dc})$  versus  $T^{-0.25}$ , exhibited in Fig. 10 (c) and (d), which verify the validity of this model. The value of  $T_0$  was computed from the slope of the VRH curve. We conclude that the transport model (VRH) may be the main low-temperature transport process. The obtained value of  $T_0$  is  $4.72 \cdot 10^8$  K and  $2.96 \cdot 10^9$  K for LNTO and LCNTO samples, respectively. Thus, the Mott temperature can be expressed by:

$$T_0 = \frac{24}{k_B \pi N(E_F)(\xi)^3} \quad (13)$$

With,  $N(E_F)$  corresponds to the density of states at the Fermi level and  $\xi$  corresponds to the localization length. Using equation (13), we estimate the density of the local state of the Fermi level. We have identified that  $N(E_F) = 3.54 \times 10^{33} \text{ eV}^{-3} \text{ cm}^{-3}$  and  $N(E_F) = 2.01 \times 10^{17} \text{ eV}^{-3} \text{ cm}^{-3}$  for LNTO and LCNTO samples, respectively. The values of  $T_0$ ,  $N(E_F)$  and  $\xi$  are classed in Table 4. The variation of the hopping energy ( $W$ ) and the mean jumping distance ( $R$ ) versus temperature is expressed by:

$$W(T) = \frac{1}{4} k T^{\frac{3}{4}} (T_0)^{\frac{1}{4}} \quad (14)$$

$$R(T) = \frac{3}{8} \xi \left(\frac{T_0}{T}\right)^{\frac{1}{4}} \quad (15)$$

The thermal variations of the  $R$  and  $W$  versus temperatures are presented in Fig. 11 (a) and (b). For these samples, it can be noticed that the variation of  $W$  and  $R$  are inversely proportional. Indeed, the jump energy rises with the rise of temperature, signaling polaronic VRH conduction dynamics in our investigated compound. While the jump distance decreases when the temperature increases. As a result, the highest jump energy is observed where the carriers can be easily released from traps, corresponding to the smallest jump length.

This investigation was helpful to understand the importance of LNTO

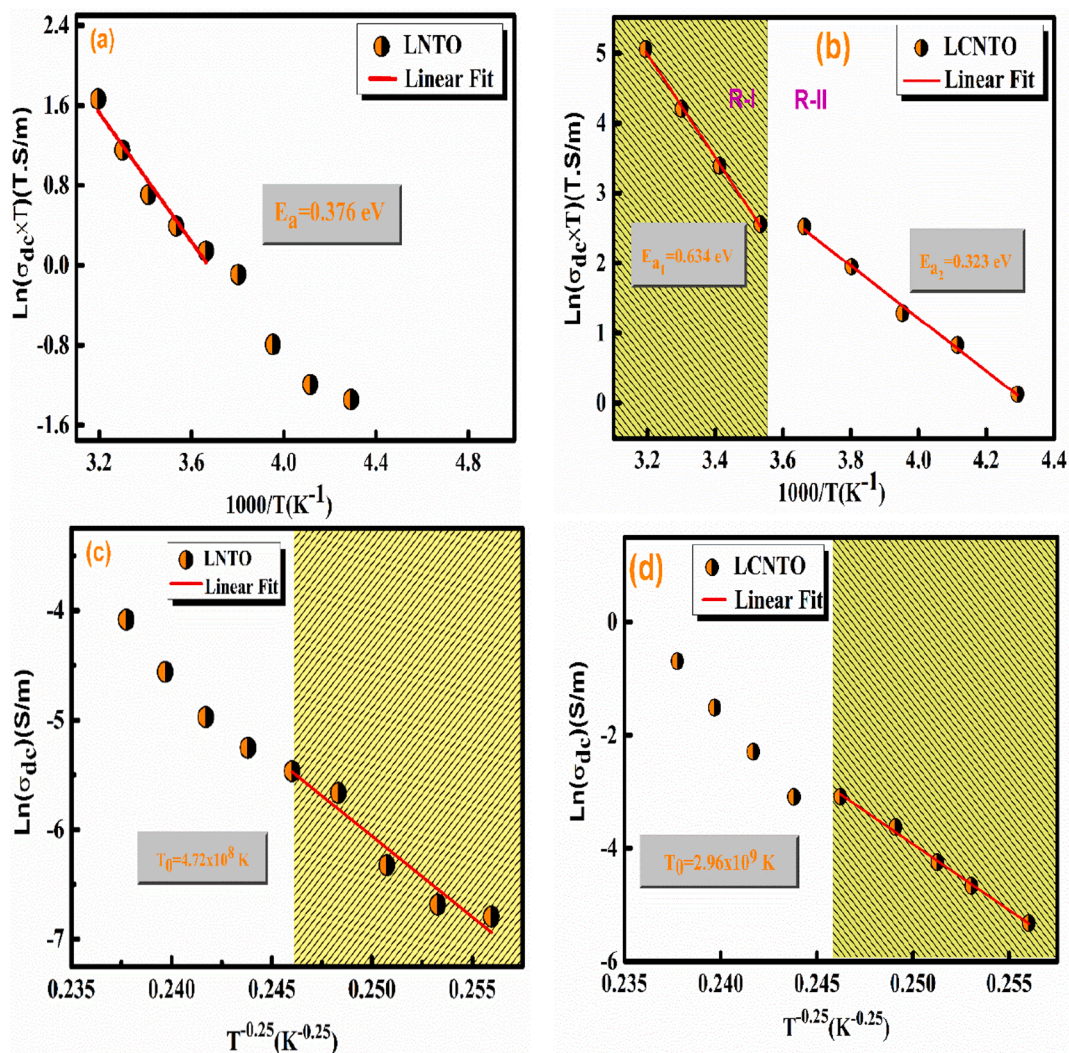


Fig. 10. The Variation of  $\text{Ln}(\sigma_{dc}.T)$  vs  $(1000/T)$  of LNTO (a) and LCNTO (b) compounds. The Variation of  $\text{Ln}(\sigma_{dc})$  vs  $(T^{-0.25})$  of LNTO (c) and LCNTO (d) compounds.

Table 4

Parameters used for NSPT and CBH model fitting for LNTO and LCNTO compounds.

Samples	$T(K)$	233 K	243 K	253 K	263 K	273 K	283 K	293 K	303 K	313 K
LNTO	$\sigma_{dc}(\text{Sm}^{-1})$	0.0011	0.0012	0.0017	0.0034	0.0042	0.0052	0.0069	0.0104	0.0168
	$A(10^{-7})$	4.030	3.460	5.048	5.159	2.338	2.862	2.239	1.753	1.473
	s	0.654	0.669	0.678	0.693	0.714	0.739	0.751	0.778	0.798
	$\sigma_{dc}(\text{Sm}^{-1})$	0.0048	0.0094	0.0143	0.0267	0.0456	0.0454	0.1012	0.2208	0.5023
LCNTO	$A(10^{-7})$	1.13	0.72	0.49	0.43	3.76	7.97	16.4	29.9	47.4
	S	1.031	1.081	1.125	1.116	1.013	0.983	1.110	1.198	1.383

and LCNTO on electrical and dielectric properties and presents details for the use of these materials in high-frequency devices. The studied materials could be potential candidates in technological applications such as electronic chips, energy storage capacitors, electrical devices, gas detection and small-volume high-performance capacitors.

#### 4. Conclusion

To conclude, this work discussed the results of structural, morphological, and electrical investigations of LNTO and LCNTO samples. The single-phase perovskite Ca substitution of La-site in  $\text{La}_{1-x}\text{Ca}_x\text{Ni}_{0.5}\text{Ti}_{0.5}\text{O}_3$

nanoparticles was prepared by the sol-gel method. X-ray diffractograms showed that this compound is pure and crystallizes in the orthorhombic system with the *Pnma* space group. The purity and morphology of nanoparticles were investigated by EDX and SEM. The electrical properties were studied using Complex Impedance Spectroscopy. The effect of space at the grain boundaries could be identified. In addition, the DC-conductivity enhances significantly with temperature confirming that our sample has a semiconductor behavior. The evolution of the “s” exponent in the function of temperature could elucidate the conduction mechanisms for both samples. On the other hand, for the LCNTO compound, the evolution of the exponent “s” as a function of temperature

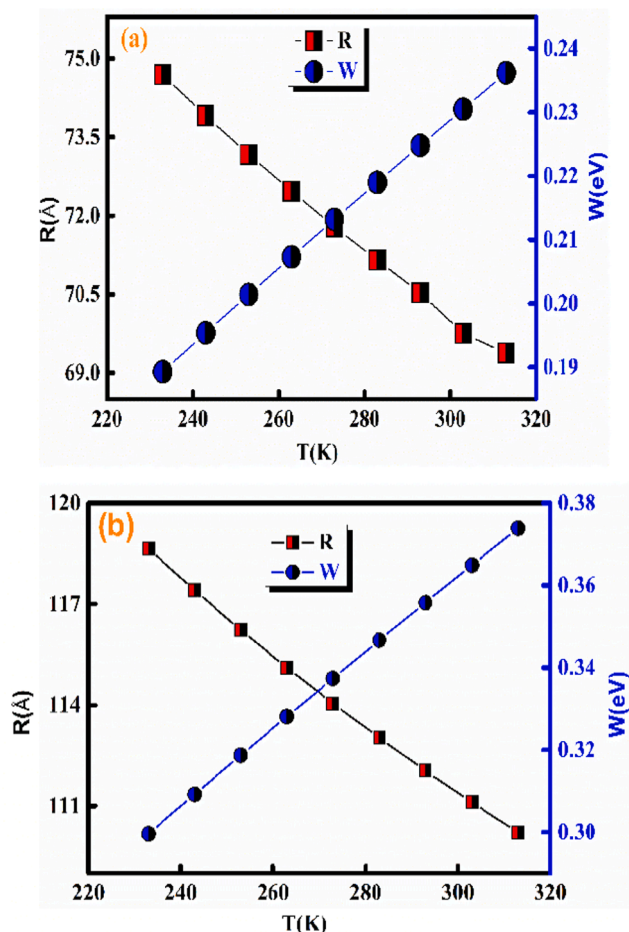


**Fig. 11.** The Variation of computed values of the activation energy  $W$  and The values of hopping range of polarons  $R$  as a function of temperature for LNT0 (a) and LCNT0 (b) compounds.

shows that (NSPT) in zone I ( $T < 255$  K) and (OLPT) in zone II ( $T > 255$  K). The dc electrical conductivity demonstrated that our compound is in agreement with the VRH model for low temperatures and the Arrhenius model in the high-temperature region. The investigated materials could be potential candidates in technological applications like energy storage devices and small-volume high-performance capacitors. In the perspective of this work, we prepare the samples described in the form of thin layers, Will study the technique VSM and Mossbauer at low temperature to enlighten the magnetic properties of these compounds and Will perform gas sensor measurements for these compounds.

#### Declaration of Competing Interest

The authors declare that they have no known competing financial interests or personal relationships that could have appeared to influence the work reported in this paper.

#### Data availability

The authors do not have permission to share data.

#### Acknowledgements

The authors acknowledge the support of the Tunisian Ministry higher education and scientific research within the framework of Tunisian-

French cooperation in the field of scientific research and technology (a project of the University Sfax-University of Angers-Hauts de France Polytechnic University). The authors would also like to thank Romain Mallet from MOLTECH-Anjou and SCIAM (University of Angers) for their help in the characterization of samples and fruitful discussions.

#### References

- [1] Alexandra navrotsky., donald j. weidner. perovskite: a structure of great interest to geophysics and materials science, geophysical monograph series, 45(2013).
- [2] Zuo-guang ye. handbook of dielectric, piezoelectric and ferroelectric materials, synthesis, properties and applications, w. p. l. cambridgeEngland(2008).
- [3] G.H. haertling.,ferroelectric ceramics: history and technology,journal of american ceramic society, 82, (1999), 797–818.
- [4] A.S.bhalla · ruyanguo · rustum roy,4(2000)3-26.
- [5] Yuanbingmao, hongjunzhou, stanislaus s. wong,synthesis, 5,2, (2010)50.
- [6] R. Hamdi, A. Tozri, M. Smari, K. Nouri, E. Dhahri, L. Bessais, J. Mol. Struct. 1175 (2019) 844–851.
- [7] A. Omri, M. Bejar, E. Dhahri, M. Es-Souni, M.A. Valente, M.P.F. Graça, L.C. Costa, J. Alloy. Comp. 536 (2012) 173–178.
- [8] K.h. Dhahri, M. Bejar, E. Dhahri, M.J. Soares, M.F.P. Graça, M.A. Sousa, J. Mater. Lett. 128 (2014) 235–237.
- [9] S. Gharbi, R. Dhahri, M. Rasheed, E. Dhahri, R. Barille, M. Rguiti, A. Tozri, M. R. Berber, Materials Science and Engineering : B. 270 (2021), 115191.
- [10] S Gharbi, R Dhahri, E Dhahri, P Sanguino, BFO Costa, R Barille, Mohamed Rguiti, and EK Hlil. Eur. Phys. J. Plus. 136(2) (2021) 1–17.
- [11] M. Yang, L. Huo, H. Zhao, S. Gao, Z. Rong, Sensors and Actuators B: Chemical 143 (2009) 111–118.
- [12] Y. Wang, X.u. Yanhong, L. Luo, Y. Ding, X. Liu, Journal of Electroanalytical Chemistry 642 (2010) 35–40.
- [13] Y. Wang, L. Luo, Y. Ding, X. Zhang, Y. Xu, X. Liu, J. of Electroanalytical Chemistry 667 (2012) 54–58.
- [14] Dhananjay.N Bhojar, Sandeep . Somvanshi, Prashant B. Kharat, A.A. Pandit, K. M. Jadhav., Physica B581(2020)411944.
- [15] S P More, M V Khedkar, S A Jadhav, Sandeep B. Somvanshi2, A V Humbe, and K M Jadhav, Journal of Physics: Conference Series 1644 (2020) 012007.
- [16] B.H. Devmunde, S.B. Somvanshi, P.B. Kharat, M.B. Solunke, Journal of Physics: Conference Series 1644 (2020), 012055.
- [17] S.B. Somvanshi, S.B. Somvanshi, P.B. Kharat, N.D. Thorat, Macromolecular Symposia 400 (2021) 00112.
- [18] G. Qin, X. Huang, J. Chen, Z. He, Powder Technol. 235 (2013) 880–885.
- [19] S. Yuvaraj, L.F. Yuan, C.T. Huei, Y.C. Tih, J. Phys. Chem. B 107 (2003) 1044–1047.
- [20] H.M. Rietveld, J. Appl. Crystallogr 2 (1969) 65–71.
- [21] L.J. Xie, J.F. Ma, Z.Q. Zhao, H. Tian, J. Zhou, Y.G. Wang, J.T. Tao, X.Y. Zhu, Colloid Surf. A 280 (2006) 232–236.
- [22] M. Wang, J. Alloy. Com. 621 (2014) 220–224.
- [23] W. Neib, A.B.J. Kharrat, M. Saadi, K. Khirouni, N. Chniba-Boudjada, W. Boujelben, ceramic compound. J. Mater. Sci. 30, (2019) 18391–18404.
- [24] M. Coskun, O. Polat, F.M. Coskun, Z. Durmus, M. Caglar, A. Turut, J. Mat.in Sci. Semi. Proces. 109 (2020) 104923-104935.
- [25] S. Nasri, A.L. Ben Hafsia, M. Tabellout and M. Megdiche, J. RSC Adv. 6 (2016) 76659-76665.
- [26] M. Shah, M. Nadeem, M. Atif, J. Appl. Phys. 112 (2012), 103718.
- [27] S. Hcini, A. Selmi, H. Rahmouni, A. Omri, M.L. Bouazizi, Ceram. Int. 43 (2017) 2529.
- [28] R. Ertugrul, A. Tataroglu, Chem. Phys. Lett. 29 (2012), 077304.
- [29] E. Barsoukov, J.R. Macdonald, Electrochemical impedance: theory, experiment, and applications (Wiley, New York, 2005).
- [30] U. Intatha, S. Eitssayeam, J. Wang, T. Tunkasiri, J. Curr. Appl. Phys. 10 (2010) 21–25.
- [31] H. Felhi, R. Lahouli, M. Smari, H. Rahmouni, K. Khirouni, E. Dhahri, J. Mol. Struct. 1179 (2019) 1–10.
- [32] A.R. James, C. Prakash, G. Prasad, J. Phys. Appl. Phys 39 (2006) 1635–1641.
- [33] J. Sharma, V.K. Parashar, D.B. Saxena, B. Sharma, Macromol. Symp 357 (2015) 38–42.
- [34] N. Chihouli, R. Dhahri, M. Bejar, E. Dharhi, L.C. Costa, M.P.F. Graça, Solid StateCommunications 151 (2011) 1331–1335.
- [35] A. Benali, M. Bejar, E. Dhahri, M.F.P. Graça, L.C. Costa, J. AlloysCompd. 653 (2015) 506.
- [36] K. Funke, J. Solid State Chem. 22 (1993) 111.
- [37] S.R. Elliott, Adv. Phys. 36 (1987) 135–217.
- [38] M. Pollak, Philos, J. Mag. 23 (1971) 519.
- [39] A. Ghosh, J. Phys. Rev. B 41 (1990) 1479.
- [40] M. Megdiche, C. Perrin-Pellegrino, M. Gargouri, J. Alloys Compd. 584 (2014) 209.
- [41] B. Swiatek-Tran, H.A. Kolodziej, A. Vogt, V.H. Tran, RSC Adv 5 (2015) 9539.
- [42] N. Sivakumar, A. Narayanasamy, J.-M. Greneche, R. Murugaraj, Y.S. Lee, J. Alloys Compd. 504 (2010) 395–402.
- [43] B. Ellis, J.P. Doumerc, P. Dordor, M. Pouchard, P. Hagenmuller, Solid State Commun. 51 (1984) 913–917.